FDTD simulation of compositionally graded HgCdTe photodetectors

FDTD simulation of compositionally graded HgCdTe photodetectors

Marco Vallone, Michele Goano, Francesco Bertazzi, Giovanni Ghione, Stefan Hanna, Detlef Eich, Heinrich Figgemeier

PII: S1350-4495(18)30778-3
DOI: https://doi.org/10.1016/j.infrared.2018.12.041
Reference: INFPHY 2830

To appear in: *Infrared Physics & Technology*

Received Date: 19 October 2018
Accepted Date: 29 December 2018

Please cite this article as: M. Vallone, M. Goano, F. Bertazzi, G. Ghione, S. Hanna, D. Eich, H. Figgemeier, FDTD simulation of compositionally graded HgCdTe photodetectors, *Infrared Physics & Technology* (2018), doi: https://doi.org/10.1016/j.infrared.2018.12.041

FDTD simulation of compositionally graded HgCdTe photodetectors

Marco Vallone[a,*], Michele Goano[a,b], Francesco Bertazzi[a,b], Giovanni Ghione[a], Stefan Hanna[c], Detlef Eich[c], Heinrich Figgemeier[c]

[a] *Politecnico di Torino, Dipartimento di Elettronica e Telecomunicazioni, Corso Duca degli Abruzzi 24, 10129 Torino, Italy*
[b] *IEIIT-CNR, corso Duca degli Abruzzi 24, 10129 Torino, Italy*
[c] *AIM Infrarot-Module GmbH, Theresienstraße 2, D-74072 Heilbronn, Germany*

Abstract

The ability to simulate HgCdTe infrared detectors with realistic alloy composition profiles is essential for their optimization. We give practical guidelines for the realization of combined three-dimensional, realistic full-wave electromagnetic and electrical modeling for the description of detectors with compositionally-graded layers, suitable to most available numerical solvers. Following the known procedure to sample the compositionally-graded layers into a number N of sublayers, we assess the effects of different choices for N, both on calculation accuracy and computational cost. Quantum efficiency spectra calculated with the proposed approach are compared with those determined through two shortcuts: ray tracing, based on classical optics, and full-wave simulation where graded layers are replaced by constant, spatially-averaged optical properties. It is shown that the former is not generally a valid alternative, since it does not address interference effects due to back-reflections, while the latter can lead to incorrect estimates of the detector cutoff wavelength.

Keywords: HgCdTe, infrared detectors, LWIR, numerical simulation, compositional grading, focal plane arrays, FDTD

*Corresponding author
Email address: marco.vallone@polito.it (Marco Vallone)

1. Introduction

The outstanding performance of the II-VI alloy HgCdTe has inspired the development of sophisticated focal-plane array (FPA) infrared photodetectors with increasingly enhanced capabilities [1, 2]. Cryogenic cooling of HgCdTe IR detectors is typically needed to decrease dark current and noise arising from several mechanisms associated with the narrow band gap of the alloy [3], and in the last fifteen years great efforts have been made to develop detectors with reduced cooling requirements. High Operating Temperature (HOT) detectors [4, 5, 6], obtained e.g. with nBn structures [7, 8, 9] or with $P^+N^-n^-N^-N$ heterostructures [10], should ultimately lead to room-temperature operation according to literature, avoiding or limiting the use of heavy and expensive cooling systems (here capital letters $N(P)$ indicate donor (acceptor) doped layers with wider band gap than the donor low-doped n^- absorber layer).

The approach of carrier-depleting the HgCdTe absorber layer using appropriate composition and doping profiles [11, 12, 13, 10] has received attention as a method of reducing the dark current, and the adoption of $Hg_{1-x}Cd_xTe$ absorbers with fine-tuned compositional grading is becoming a standard option also in order to optimize the quantum efficiency (QE) [14]. Thus, the capability to numerically predict the performance of FPA infrared detectors with realistic state-of-the-art composition profiles is a present need and an essential step towards their development.

Most commercial three-dimensional (3D) device simulators allow to handle the *electrical* modeling of photodetectors, even if compositionally graded. Nevertheless, in order to solve the electrical problem under illumination, the carrier photogeneration rate distribution $G_{\rm opt}$ ensuing from illumination must be evaluated. The propagation of electromagnetic waves in any medium is completely described by the solution of Maxwell's equations, a task that in FPA detectors can be numerically addressed by full-wave techniques such as the Finite Difference Time Domain method (FDTD) [15, 16, 17]. When the electromagnetic solution is known, $G_{\rm opt}$ easily follows (see Sec. 3).

However, when compositionally graded photodetectors are considered, the full-wave calculation of $G_{\rm opt}$ may require the development of particular techniques, and also in very recent works [18, 14] ray tracing [19] or even simpler methods based on

Beer's absorption law [20, Sec. 1.6.2] have been employed to this end, neglecting the wavelike nature of infrared radiation.

Scope of this work is to give practical guidelines in order to obtain an electromagnetic solution by FDTD for compositionally graded HgCdTe photodetectors, where the Cd mole fraction x gradually changes along the growth direction, investigating to what extent different handlings of the x-grading affect the accuracy of the solution. Our purpose is also to point out what can be lost when neglecting the detector compositional grading in the calculation of G_{opt}, for example by averaging x in the graded regions. A ray tracing implementation that correctly manages compositional grading and internal light back-reflections but is intrinsically unable to describe interference and diffraction [21] has been used as an additional reference.

The manuscript is organized as follows. In Section 2 a single pixel of a 3D detector is described as case study. Section 3 describes the method we propose to obtain the electromagnetic solution by FDTD. Simulated QE spectra are shown, compared and discussed in Section 4. Finally, Section 5 summarizes the main outcomes of this study.

2. Single pixel detector

We performed combined optical and electrical 3D simulations considering a long-wavelength infrared (LWIR) single pixel of a planar HgCdTe-based FPA photodetector, identified by a $d \times d \times t$ cell, where $d = 10\,\mu$m is the pixel size and t is the total epitaxial thickness.

Since the main scope of the present work is methodological, in order to test the proposed approach we chose an epitaxial structure inspired by the literature, very similar to [14]. A two-dimensional (2D) scheme of the adopted doping and composition profiles is shown in Fig. 1, where an inset showing the 3D single pixel layout is also reported. Above as CdTe substrate, a wide-bandgap n-$Hg_{0.6}Cd_{0.4}Te$ layer was grown, doped with donor concentration $N_{\mathrm{D}} = 5 \times 10^{17}$ cm^{-3}. It is followed by a 5 μm thick, low donor-doped, narrow-bandgap HgCdTe absorber layer ($N_{\mathrm{D}} = 1 \times 10^{14}$ cm^{-3}), and by another wide-bandgap $Hg_{0.6}Cd_{0.4}Te$ layer, with the same low donor concentration. The $n-p$ photodiode junction was defined by simulating an ion implantation, yielding

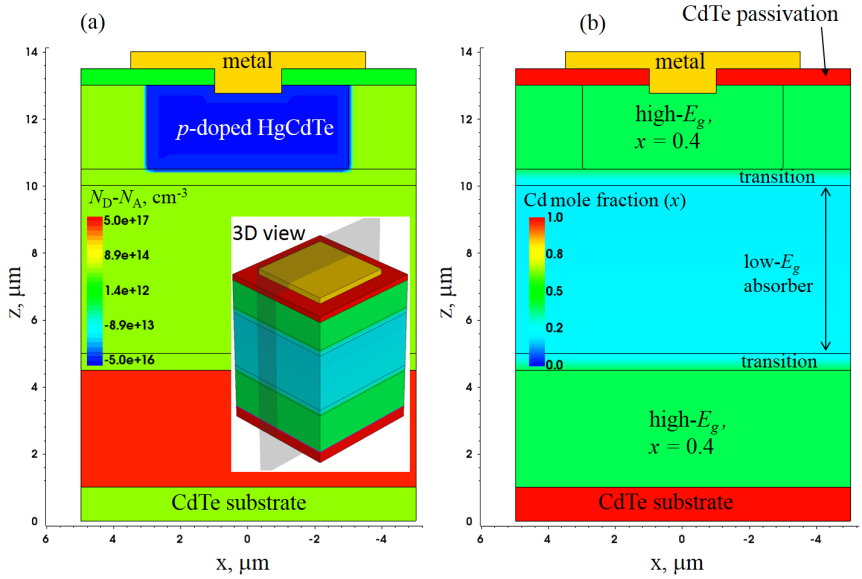

Figure 1: (a) 2D section of a single pixel with the doping profile $N_D - N_A$. In the inset, the 3D single pixel is shown. (b) 2D section of a single pixel, showing the z-dependent Cd mole fraction of the $Hg_{1-x}Cd_xTe$ heterostructure, where z is the growth direction. In Fig. 2 more details are given.

an error-function-shaped acceptor density N_A ranging from $5 \times 10^{16}\,\mathrm{cm}^{-3}$ just below the bias contact to virtually zero at the *p-n* junction in $\approx 2.5\,\mu$m.

In [14], the absorber layer was given a graded composition, varying the Cd mole fraction from $x = 0.21$ to $x = 0.19$, from its lower to its upper interface, in order to maintain a constant peak wavelength at the temperature of operation. We adopted this choice not for this particular purpose, but just as a literature example of compositionally graded absorber. Still in [14], in order to increase realism two $0.5\,\mu$m thick transition regions with linear compositional grading connect the two high-E_g regions to the low-E_g absorber layer (where E_g is the bandgap). In order to test the proposed model in more critical conditions, a variant was also considered, giving the absorber a steeper compositional grading, from $x = 0.25$ to $x = 0.19$. For brevity, in the present work we identify the two variants respectively as the *standard* and the *steeper* one, and in Fig. 2, the Cd mole fraction and the dopant concentrations along a one-dimensional (1D) vertical cutline at center pixel are shown, for the two considered variants. The bias

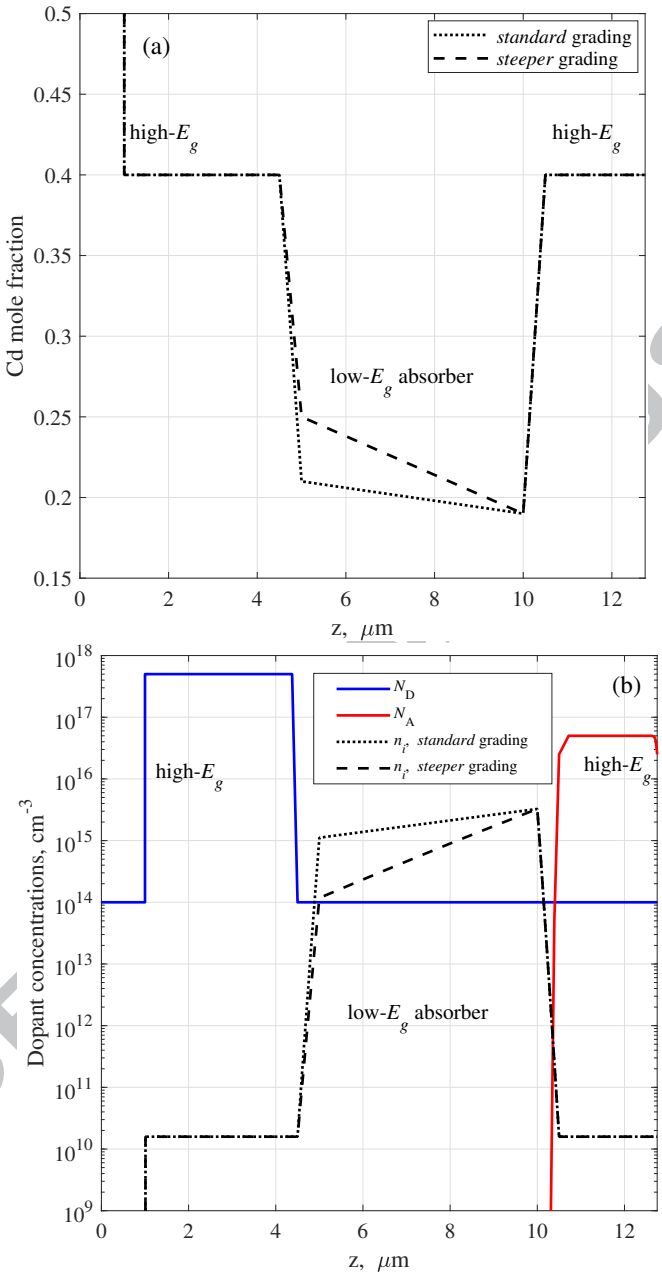

Figure 2: (a) Cd mole fraction for the *standard* and *steeper* variants of the absorber. (b) Dopant concentrations N_D and N_A along a 1D vertical cutline at center pixel. The intrinsic density n_i for $T = 140$K is also shown as black dotted and dashed lines for the two variants.

contact is connected to the p-doped region through a square metallic layer $7\mu\text{m} \times 7\mu\text{m}$ wide, partly extending over a $0.3\,\mu\text{m}$ thick CdTe passivation layer that covers the upper face of the FPA's single pixel.

The geometry, doping and composition profiles were defined employing the Sentaurus 3D numerical simulator by Synopsys [22], also employed to perform the electrical simulations as described in Sec. 4.

3. Electromagnetic simulations

In order to obtain the photogeneration rate G_{opt} for a given illumination, we adopted the FDTD approach [17], solving Maxwell's equations for the electric and magnetic fields $\vec{E}$ and $\vec{H}$, discretized on a cubic grid known as the Yee grid [15]. For validation purpose, we employed and compared the results obtained by two commercial codes, the Electromagnetic Wave (EMW) solver [22], and the RSoft FullWAVE [23], both integrated in the same Synopsys simulation suite Sentaurus Workbench [22]. The computational box includes air layers located above and below the pixel, and the optical boundary conditions (BC) along the upper and lower sides of the box are absorbing (this is obtained with convolutional perfectly matching layers [16]), while periodic optical BCs are applied along the lateral sides of the computational box, in order to exploit symmetry and obtain a simulation equivalent to a FPA. In the FDTD model, the material properties are represented by the electric permittivity and conductivity ε and σ, calculated from the material complex refractive index $\hat{n} = n + i\kappa$ as

$$\begin{aligned} \varepsilon &= n^2 - \kappa^2 = n^2 - \left(\frac{\alpha\lambda}{4\pi}\right)^2 \\ \sigma &= \frac{n\alpha}{\mu_0 c}, \end{aligned} \tag{1}$$

where λ is the wavelength, μ_0 is the vacuum magnetic permeability, c is the speed of light in vacuum, and $\alpha = 4\pi\kappa/\lambda$ is the absorption coefficient. The absorbed photon density A_{opt} (number of absorbed photons per unit volume and time) can be evaluated as the divergence of the time-averaged Poynting vector $\langle\vec{S}\rangle$ [24, 25, 26, 27]

$$A_{\text{opt}} = -\frac{\vec{\nabla}\cdot\langle\vec{S}\rangle}{h\nu} = \frac{1}{2h\nu}\sigma|\vec{E}|^2, \tag{2}$$

where $h\nu$ is the photon energy. The optical generation rate distribution G_{opt} into the pixel due to interband optical absorption is given by $G_{\text{opt}} = \eta A_{\text{opt}}$, where the quantum yield η, defined as the fraction of absorbed photons which are converted to photogenerated electron-hole pairs, was assumed to be unitary (see calculation examples for monochromatic [21, 28] and for broadband illumination [29, 30, 31], all following the FDTD method. Similar methods were also applied with success to other types of photodetectors, see e.g. [32, 33], and in simpler one-dimensional [34] and two-dimensional modeling descriptions [35].

In all simulations, we set a lattice temperature $T = 140\,\text{K}$, the HgCdTe optical properties were described through the models and parameters reported in [28, Table I], and the contact metallizations were treated as Perfect Electric Conductors (PEC) [17].

3.1. Discretization of compositionally graded regions

The solution of the electromagnetic problem for detectors with arbitrary composition profile may not be straighforward, since not all simulators manage a compositional grading, neither as analytic function, nor as external file, requiring instead to define the detector geometry as a stack of layers each with uniform optical properties. However, since the considered composition profile only varies along z (the growth direction), the idea was to sample the profile, converting it to a staircase, discretizing consequently the detector itself into a large stack of layers, each with uniform values for n and κ.

In order to test the feasibility of this general idea, we implemented the method in both considered simulators, without taking advantage of particular solutions of the compositional grading problem, possibly implemented by the simulator manufacturer.

Exploiting the planarity of the structure, the simulation flow includes a Tcl [36] script that builds the device geometry, discretizing the low-E_g absorber layer and the two low-to-high-E_g transition regions into N sublayers each. This step is common to both simulators, since they are able to read the same geometry boundary files. Then, starting from the adopted expressions for the complex refractive index [28, Table I], another Tcl script converts the linear grading of the Cd mole fraction x to a staircase x_i, $i = 0,...,N-1$, building N tables $(\lambda_m, n_m, \kappa_m)_i$, for values $\lambda_m \in [1,20]\,\mu$m, separated by $0.1\,\mu$m. Regarding the other regions with uniform composition (the sub-

strate, high-E_g, and passivation regions), the usual approach was followed, building one $(\lambda_m, n_m, \kappa_m)$ table for each of them. In this way, for a given operating wavelength $\lambda \in \{\lambda_m\}$, the N look-up tables $(\lambda_m, n_m, \kappa_m)_i$ provide the desired discretized n- and κ-profiles. In the end, the described Tcl script produces a set of material libraries as ASCII files, one of each layer or sublayer, including them appropriately in the material library of both simulators, only respecting the required file formats they separately need.

3.2. Results

As an example and considering the *standard* variant, in Fig. 3(a–c) the discretized n and κ distributions are shown for $N = 10$, calculated for $\lambda = 9\mu$m. For appreciating more quantitatively their variation across the compositionally graded regions, in Fig. 3(d,e) the n and κ profiles are shown along a vertical 1D cutline. The optical grid was chosen with a spacing of 10 nm in the z-direction, and 25 nm in the x,y-directions.

Our starting point consisted in performing a FDTD simulation for an illuminating plane wave with $\lambda = 9\mu$m. The optical source was located in air, and the detector was illuminated from below, with wavevector orthogonal to the plane z=0, setting an optical flux P_{in} = 1 mW cm^{-2}. The rate A_{opt} obtained for the case $N = 10$ by the EMW solver is plotted in Fig. 4(a-c) on 2D cutplanes y = 0 and y = 4 on appropriate scales, to point up the reflections effect due to the metallization on the photogeneration distribution. Then, we repeated the simulation still with EMW, for $N = 5, 10, 15, 30$ and, in order to validate the proposed computational method and discretization algorithm, the same simulation was also performed by FullWAVE for $N = 10$. The results are plotted in Fig. 4(d, e), along a vertical 1D cutline at x = y = 4 μm. The four distributions obtained by EMW are apparently very similar, and the computational time does not depend much on the choice of N ($\approx$ 30 minutes on our servers), provided we employ the same spatial grid. The FullWAVE solver yields a solution differing a little more from them, but still following the same overall behavior.

4. Electrical simulations

For a given illumination, in the drift-diffusion framework G_{opt} enters as a source term in the continuity equations for the electron and hole current densities $J_{n,p}$, that can be solved as outlined e.g. in [21, 28, 30], in order to obtain the current under illumination I and in dark I_{dark}. The photocurrent follows as $I_{\text{ph}} = I - I_{\text{dark}}$ and the

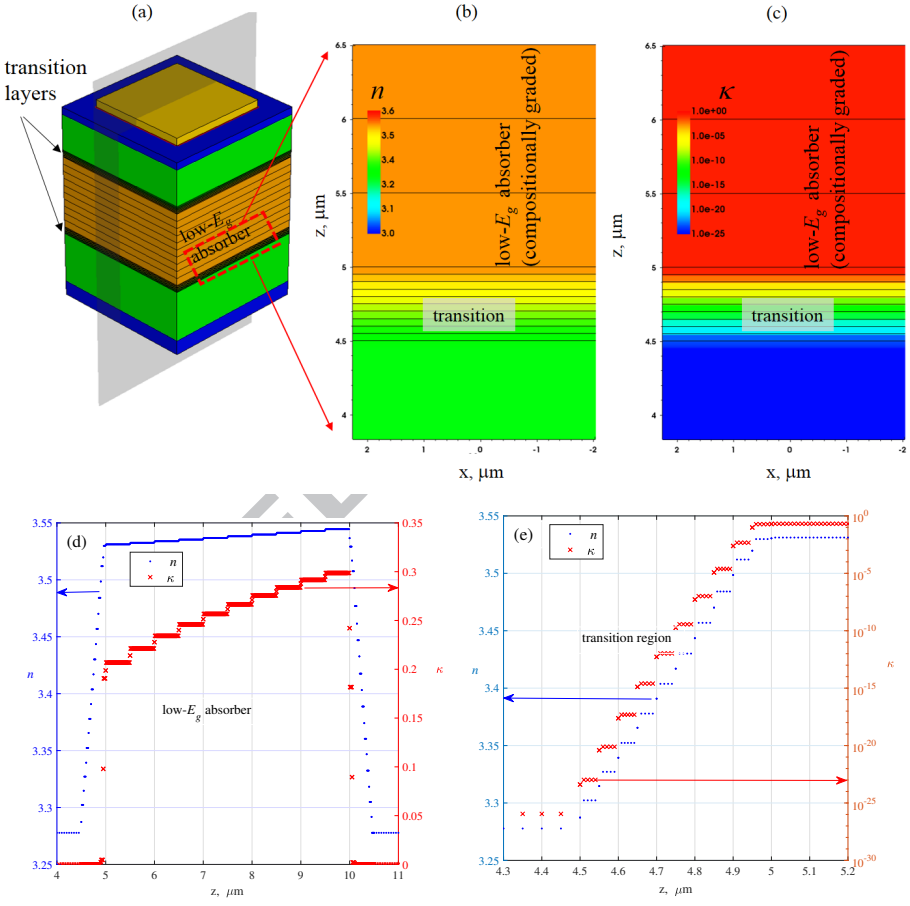

Figure 3: *Standard* variant: (a) 3D overall view of a single pixel, showing the discretization into $N = 10$ sublayers of the low-E_g absorber region and the two transition regions. In panels (b) and (c), the real and imaginary parts of the complex refractive index n and κ, calculated for $T = 140$K and $\lambda = 9\mu$m, are shown for a small portion of a vertical 2D cutplane (the dashed portion shown in panel (a)). In panels (d, e) n and κ are shown along a vertical 1D cutline at center pixel: panel (d) is centered across the low-E_g absorber region, and panel (e) across one of the two transition regions.

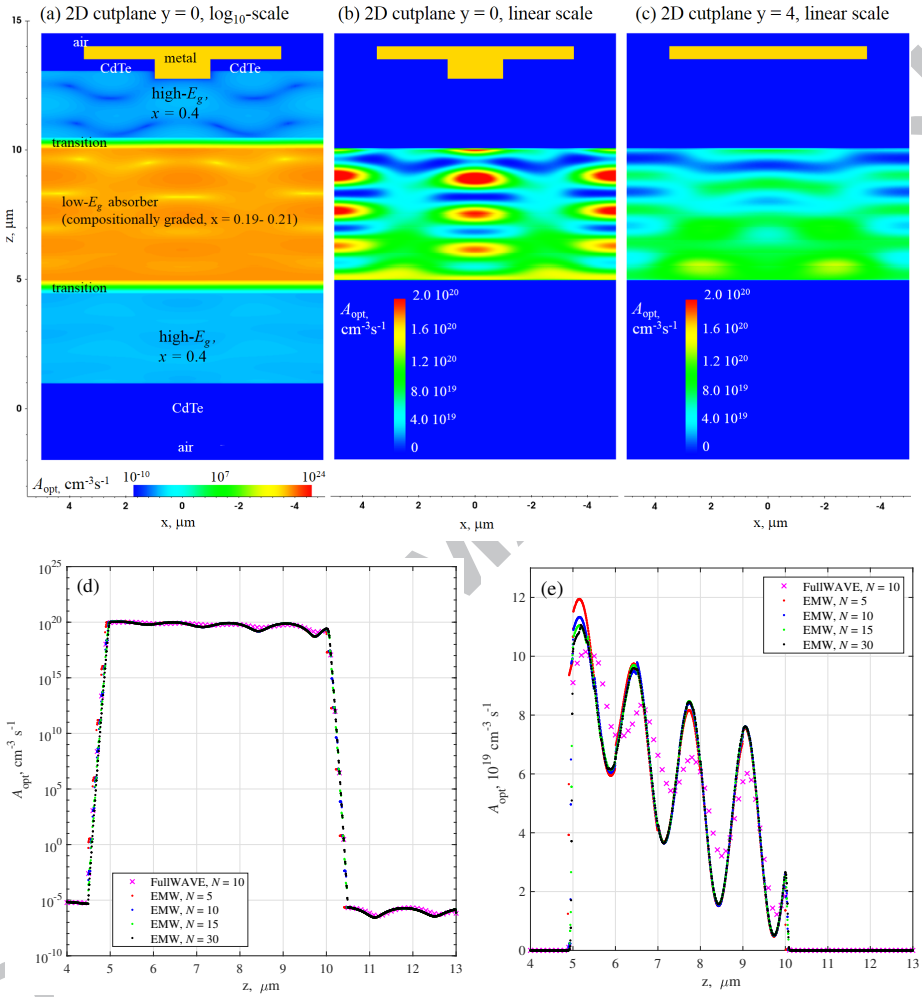

Figure 4: *Standard* variant: A_{opt} in the 2D cutplane y = 0, obtained for the case $N = 10$ by the EMW solver for $\lambda = 9\,\mu$m, in logarithmic (a) and linear (b) scale. In panel (c) A_{opt} is shown in the 2D cutplane y = 4 in linear scale, to point up the reflections effect due to the metallization on the photogeneration distribution. In the panels (d) and (e), A_{opt} is shown on a logaritmic and linear scale along a vertical 1D cutline at x = y = $4\,\mu$m, for all the considered discretization cases $N = 5, 10, 15, 30$ - EMW, compared with the case $N = 10$ - FullWAVE, for the reciprocal validation of the method implemented in the two electromagnetic solvers.

quantum efficiency as $\mathrm{QE} = I_{\mathrm{ph}}/(qN_{\mathrm{phot}})$, where q is the elementary charge and N_{phot} is the photon flux impinging the illuminated face. To this end, the detector in Fig. 1 was discretized into $\approx 1.48 \times 10^5$ elements with a meshing tool which generates a denser grid in regions where gradients of current density, electric field, free charge density and material composition are present. The HgCdTe properties were described through the models reported in [28], taking into account the composition, doping, and temperature dependence of the HgCdTe alloy. The Shockley-Read-Hall (SRH) recombination processes were modeled as in [37, 20, 38] considering a lifetime around 2 μs, neglecting instead trap-assisted or band-to-band tunneling processes [39, 40]. Fermi-Dirac statistics and incomplete dopant ionization were taken into account, with activation energies for HgCdTe alloys estimated according to [41, 42]. Electric contacts were treated as Ohmic with zero resistance, where charge neutrality and equilibrium were assumed. Ideal Neumann BCs were applied to the outer boundaries of the array, and the drift-diffusion equations were solved by the Finite Box (FB) method, setting $T = 140$K and driving the detector at 0.5 V of reverse bias.

Compositional grading is not an issue for electrical simulations, since the nominal HgCdTe composition profile shown in Fig. 2(a) is evaluated at each point of the electrical grid, and the N-sublayers discretization is not required. On the other hand, since the grading imposed to develop particular techniques to solve the electromagnetic problem, it is interesting to compare the QE spectra obtained when G_{opt} is evaluated *a*) following the described N-sublayers discretization method, and *b*) averaging n and κ in the graded regions, to see what we loose neglecting the grading in the electromagnetic modeling. In addition, *c*) the same calculation was done following the ray tracing method, and the obtained QE spectra are shown for the three cases in Fig. 5. The spectra for cases *a*) and *b*) are quite similar, due to the small variation of the HgCdTe composition in the absorber. Conversely, the spectrum for ray tracing, case *c*), is significantly different close to the cutoff wavelength (usually defined as the λ value where the QE drops to one half of its maximum value). In fact, FDTD is able to describe interference effects, particularly relevant because of the large metallization of the bias contact, acting as a reflector to increase QE. On the contrary, ray tracing does not address the wavelike nature of radiation: an extended discussion with several

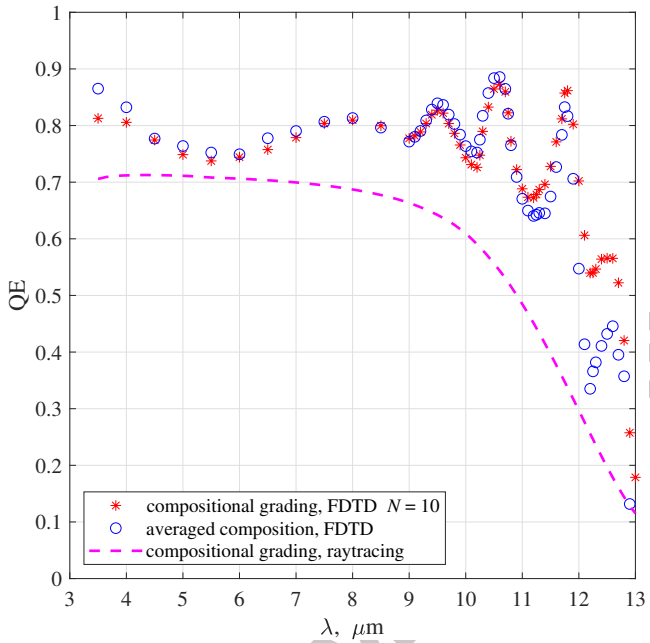

Figure 5: *Standard* variant calculated QE spectra, comparing: FDTD spectrum obtained with the described discretization scheme, with $N = 10$ (*stars*), or averaging the n and κ in each graded region (*circles*). Dashed line, spectrum obtained with the ray tracing method.

comparisons between FDTD and ray tracing results can be found in [21].

Similar electromagnetic and electrical simulations were repeated for the *steeper* variant of the detector, in order to assess the effect of the compositional grading steepness in the absorber, and the obtained QE spectra are shown in Fig. 6, for the three electromagnetic computational methods. In this case, it is evident that, neglecting the grading in the electromagnetic modeling (case *b*)), the overall cutoff wavelenght would be wrongly estimated, although the gradient of the composition profile in the absorber is still moderate. Instead the two solutions are quite similar when the material is more absorbing and the effect of the compositional grading looses importance, but this happens for $\lambda < 8\,\mu$m, *i.e.* out of the LWIR window. The ray tracing spectrum lies in between the two FDTD solutions, but close to the cutoff wavelength the ray tracing method still underestimates the QE by a factor of two, precisely because it neglects any interference effects, particularly important when the material becomes less absorb-

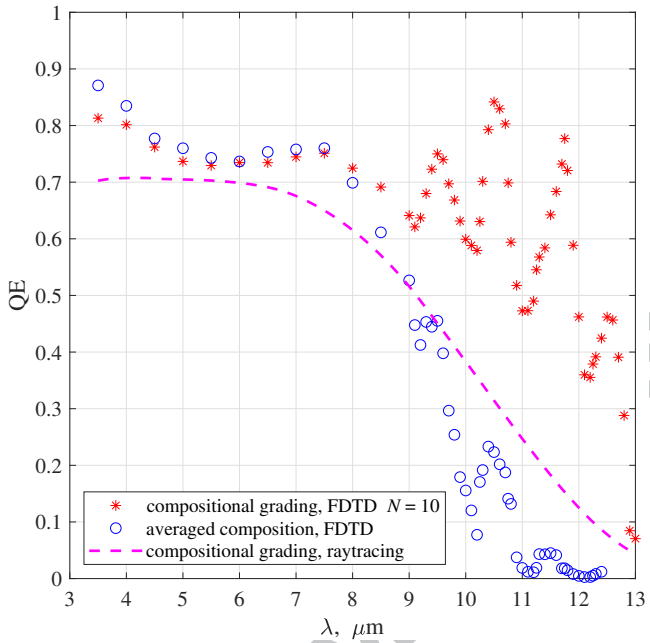

Figure 6: *Steeper* variant calculated QE spectra, comparing: FDTD spectrum obtained with the described discretization scheme, with $N = 10$ (*stars*), or averaging the n and κ in each graded region (*circles*). Dashed line, spectrum obtained with the ray tracing method.

ing [21].

5. Conclusions

We investigated the optical and electrical response of compositionally graded HgCdTe planar photodetector by means of a combined FDTD-FB approach, giving practical guidelines for the implementation of a three-dimensional modeling method particularly suitable for electromagnetic solvers that do not manage compositional grading directly. In the present case, a linear grading was considered as an example, but in principle the method can be easily applied to a wide choice of profiles.

On this purpose, we assessed the effect of different choices for the number of sublayers N adopted to sample a compositionally graded region. N should be large enough to guarantee a small reflection coefficient R_i between adjacent sublayers in the absorber's graded region. It is easy to verify that, in the considered cases, its approximate

estimate as $R_i \approx (n_{i+1} - n_i)^2/(n_{i+1} + n_i)^2$ (Fresnel law), valid for normal incidence, assures $R_i < 10^{-4}$ also for small values of N. We also observed that the value of N has a small impact on the computational cost of the simulation. Consequently, it is recommended to choose a value large enough to sample the absorption coefficient profile $\alpha(z)$ properly, in order to get an accurate estimate of the detector's cutoff wavelength, to which end some tests are generally needed.

Another important point was to assess the possibility to consider simpler approximations, like averaging x in the region when the grading is present, or considering the ray tracing method to solve the electromagnetic problem. We pointed out that a $Hg_{1-x}Cd_xTe$ composition profile cannot be approximated, in general, by simply averaging x in the graded region, since also moderate compositional gradients of x may lead to incorrect predictions of quantum efficiency spectra and cutoff wavelengths. In fact, if for the *standard* variant Fig. 5 shows that averaging x in the absorber is still an acceptable approximation, as soon as moderately steeper profiles are considered, the approximation loses precision, as shown in Fig. 6 for the *steeper* variant.

Regarding the ray tracing approach, it has not proved to be a valid alternative, not addressing the interference effects due to back-reflections. Similar conclusions were drawn in [25], which compared a FDTD calculation with a result obtained considering a simple exponential decay of the photon flux inside the device.

The greatest sources of back-reflections are the interfaces with metallizations, which are assumed to be totally reflecting. The effect is particularly relevant when large contact metallizations are present, leading to absorption enhancement close to cutoff wavelength owing to spatial resonances and cavity effects [21].

Future work will consist in simulating compositionally graded FPA detectors, single color or multi-color [1, 43, 44, 2], illuminated by extended, nonmonochromatic sources. Incoherent light, especially if produced by broadband (e.g. blackbody) source, results in less prominent resonance effects, as described in Ref. [30] for simpler photodetectors without compositional grading, and it would be interesting to extend that study to detectors with more general composition profiles. Finally, we stress that the presented modeling approach is suitable to be applied to any electromagnetic simulator not designed to directly manage compositionally graded regions.

References

[1] A. Rogalski, J. Antoszewski, L. Faraone, Third-generation infrared photodetector arrays, J. Appl. Phys. 105 (9) (2009) 091101. doi:10.1063/1.3099572.

[2] P. Martyniuk, J. Antoszewski, M. Martyniuk, L. Faraone, A. Rogalski, New concepts in infrared photodetector designs, Appl. Phys. Rev. 1 (2014) 041102. doi:10.1063/1.4896193.

[3] M. A. Kinch, Fundamental physics of infrared detector materials, J. Electron. Mater. 29 (6) (2000) 809–817. doi:10.1007/s11664-000-0229-7.

[4] T. Ashley, C. T. Elliott, Model for minority carrier lifetimes in doped HgCdTe, Electron. Lett. 21 (10) (1985) 451–452. doi:10.1049/el:19850321.

[5] C. T. Elliott, Non-equilibrium modes of operation of narrow-gap semiconductor devices, Semiconductor Sci. Tech. 5 (35) (1990) S30. doi:10.1088/0268-1242/5/3S/008.

[6] P. Martyniuk, A. Rogalski, HOT infrared photodetectors, Opto-Electron. Rev. 21 (2) (2013) 239–257. doi:10.2478/s11772-013-0090-x.

[7] S. Maimon, G. W. Wicks, *nBn* detector, an infrared detector with reduced dark current and higher operating temperature, Appl. Phys. Lett. 89 (15) (2006) 151109. doi:10.1063/1.2360235.

[8] A. M. Itsuno, J. D. Phillips, S. Velicu, Predicted performance improvement of Auger-suppressed HgCdTe photodiodes and *p-n* heterojunction detectors, IEEE Trans. Electron Devices 58 (2) (2011) 501—507. doi:10.1109/TED.2010.2093577.

[9] A. M. Itsuno, J. D. Phillips, S. Velicu, Mid-wave infrared HgCdTe nBn photodetector, Appl. Phys. Lett. 100 (16) (2012) 161102. doi:10.1063/1.4704359.

[10] J. Schuster, W. E. Tennant, E. Bellotti, P. S. Wijewarnasuriya, Analysis of the Auger recombination rate in $P^+N^-n^-N^-N$ HgCdTe detectors for HOT applica-

tions, in: Infrared Technology and Applications XLII, Vol. 9819, Proceedings of the SPIE, 2016, p. 98191F. doi:10.1117/12.2224383.

[11] W. Lei, J. Antoszewski, L. Faraone, Progress, challenges, and opportunities for HgCdTe infrared materials and detectors, Appl. Phys. Rev. 2 (4) (2015) 041303. doi:10.1063/1.4936577.

[12] P. Martyniuk, W. Gawron, J. Pawluczyk, A. Keblowski, ¡p. Madejezyk, A. Rogalski, Dark current suppression in HOT LWIR HgCdTe heterostructures operating in non-equilibrium mode, J. Infrared Millim. Waves 34 (2015) 385–390. doi:10.11972/j.issn.1001-9014.2015.04.001.

[13] J. Schuster, R. DeWames, P. S. Wijewarnasurya, Dark currents in a fully-depleted LWIR HgCdTe *P*-on-*n* heterojunction: analytical and numerical simulations, J. Electron. Mater. 46 (11) (2017) 6295–6305. doi:10.1007/s11664-017-5736-x.

[14] A. Rogalski, M. Kopytko, P. Martyniuk, Performance prediction of p-i-n HgCdTe long-wavelength infrared HOT photodiodes, Appl. Opt. 57 (18) (2018) D11–D18. doi:10.1364/AO.57.000D11.

[15] K. Yee, Numerical solution of initial boundary value problems involving Maxwell's equations in isotropic media, IEEE Trans. Antennas Propagation 14 (3) (1966) 302–307. doi:10.1109/TAP.1966.1138693.

[16] J.-P. Berenger, A perfectly matched layer for the absorption of electromagnetic waves, J. Comp. Phys. 114 (2) (1994) 185–200. doi:10.1006/jcph.1994.1159.

[17] D. Vasileska, S. M. Goodnick, G. Klimeck, Computational Electronics. Semiclassical and Quantum Device Modeling and Simulation, CRC Press, Boca Raton, FL, 2010.

[18] P. Martyniuk, P. Madejczyk, M. Kopytko, W. Gawron, J. Rutkowski, Utmost response time of long-wave HgCdTe photodetectors operating un-

der zero voltage condition, Opt. Quantum Electron. 50 (1) (2018) 1–17. doi:10.1007/s11082-017-1278-y.

[19] G. H. Spencer, M. V. R. K. Murty, General ray-tracing procedure, J. Opt. Soc. Amer. 52 (6) (1962) 672–676. doi:10.1364/JOSA.52.000672.

[20] S. M. Sze, K. K. Ng, Physics of Semiconductor Devices, 3rd Edition, John Wiley & Sons, Hoboken, NJ, 2007.

[21] M. Vallone, M. Goano, F. Bertazzi, G. Ghione, W. Schirmacher, S. Hanna, H. Figgemeier, Comparing FDTD and ray tracing models in the numerical simulation of HgCdTe LWIR photodetectors, J. Electron. Mater. 45 (9) (2016) 4524–4531. doi:10.1007/s11664-016-4481-x.

[22] Synopsys, Inc., Mountain View, CA, Sentaurus Device User Guide. Version M-2017.09 (Sep. 2017).

[23] Synopsys, Inc., Inc., Optical Solutions Group, Ossining, NY, RSoft FullWAVE User Guide, v2017.03 (2017).

[24] M. Born, E. Wolf, Principles of Optics. Electromagnetic Theory of Propagation, Interference and Diffraction of Light, 7th Edition, Cambridge University Press, Cambridge, U.K., 1999.

[25] C. Keasler, E. Bellotti, Three-dimensional electromagnetic and electrical simulation of HgCdTe pixel arrays, J. Electron. Mater. 40 (8) (2011) 1795–1801. doi:10.1007/s11664-011-1644-7.

[26] J. Liang, W. Hu, Z. Ye, L. Liao, Z. Li, X. Chen, W. Lu, Improved performance of HgCdTe infrared detector focal plane arrays by modulating light field based on photonic crystal structure, J. Appl. Phys. 115 (18) (2014) 184504. doi:10.1063/1.4876227.

[27] O. Akın, H.-V. Demir, High-efficiency low-crosstalk dielectric metasurfaces of mid-wave infrared focal plane arrays, Appl. Phys. Lett. 110 (2017) 143106. doi:10.1063/1.4979664.

[28] M. Vallone, M. Goano, F. Bertazzi, G. Ghione, W. Schirmacher, S. Hanna, H. Figgemeier, Simulation of small-pitch HgCdTe photodetectors, J. Electron. Mater. 46 (9) (2017) 5458–5470. doi:10.1007/s11664-017-5378-z.

[29] M. Vallone, A. Palmieri, M. Calciati, F. Bertazzi, F. Cappelluti, G. Ghione, M. Goano, S. Hanna, H. Figgemeier, R. Scarmozzino, E. Heller, M. Bahl, Broadband 3D optical modeling of HgCdTe infrared focal plane arrays, in: 17th International Conference on Numerical Simulation of Optoelectronic Devices (NUSOD 2017), Copenhagen, Denmark, 2017, pp. 205–206. doi:10.1109/NUSOD.2017.8010063.

[30] M. Vallone, A. Palmieri, M. Calciati, F. Bertazzi, F. Cappelluti, G. Ghione, M. Goano, M. Bahl, E. Heller, R. Scarmozzino, S. Hanna, D. Eich, H. Figgemeier, Non-monochromatic 3D optical simulation of HgCdTe focal plane arrays, J. Electron. Mater. 47 (10) (2018) 5742–5751. doi:10.1007/s11664-018-6424-1.

[31] M. Vallone, M. Goano, F. Bertazzi, G. Ghione, S. Hanna, D. Eich, H. Figgemeier, Diffusive-probabilistic model for inter-pixel crosstalk in HgCdTe focal plane arrays, IEEE J. Electron Devices Soc. 6 (1) (2018) 664–673. doi:10.1109/JEDS.2018.2835818.

[32] M. Vallone, A. Palmieri, M. Calciati, F. Bertazzi, M. Goano, G. Ghione, F. Forghieri, 3D physics-based modelling of Ge-on-Si waveguide *p-i-n* photodetectors, in: 17th International Conference on Numerical Simulation of Optoelectronic Devices (NUSOD 2017), Copenhagen, Denmark, 2017, pp. 207–208. doi:10.1109/NUSOD.2017.8010064.

[33] A. Palmieri, M. Vallone, M. Calciati, A. Tibaldi, F. Bertazzi, G. Ghione, M. Goano, Heterostructure modeling considerations for Ge-on-Si waveguide photodetectors, Opt. Quantum Electron. 50 (2) (2018) 71. doi:10.1007/s11082-018-1338-y.

[34] S. Mouzali, S. Lefebvre, S. Rommeluère, Y. Ferrec, J. Primot, Optical-based spectral modeling of infrared focal plane arrays, Infrared Phys. Tech. 77 (2016) 351–359. doi:10.1016/j.infrared.2016.06.024.

[35] O. Gravrand, S. Gidon, Electromagnetic modeling of *n*-on-*p* HgCdTe back-illuminated infrared photodiode response, J. Electron. Mater. 37 (9) (2008) 1205–1211. doi:10.1007/s11664-008-0478-4.

[36] J. Ousterhout, K. Jones, Tcl and Tk toolkit, Addison-Wesley Professional, 2010.

[37] W. Shockley, W. T. Read, Statistics of the recombinations of holes and electrons, Phys. Rev. 87 (5) (1952) 835–842. doi:10.1103/PhysRev.87.835.

[38] M. Vallone, M. Mandurrino, M. Goano, F. Bertazzi, G. Ghione, W. Schirmacher, S. Hanna, H. Figgemeier, Numerical modeling of SRH and tunneling mechanisms in high-operating-temperature MWIR HgCdTe photodetectors, J. Electron. Mater. 44 (9) (2015) 3056–3063. doi:10.1007/s11664-015-3767-8.

[39] M. Mandurrino, G. Verzellesi, M. Goano, M. Vallone, F. Bertazzi, G. Ghione, M. Meneghini, G. Meneghesso, E. Zanoni, Trap-assisted tunneling in InGaN/GaN LEDs: experiments and physics-based simulation, in: 14th International Conference on Numerical Simulation of Optoelectronic Devices (NUSOD 2014), Palma de Mallorca, Spain, 2014, pp. 13–14. doi:10.1109/NUSOD.2014.6935332.

[40] M. Mandurrino, M. Goano, M. Vallone, F. Bertazzi, G. Ghione, G. Verzellesi, M. Meneghini, G. Meneghesso, E. Zanoni, Semiclassical simulation of trap-assisted tunneling in GaN-based light-emitting diodes, J. Comp. Electron. 14 (2) (2015) 444–455. doi:10.1007/s10825-015-0675-3.

[41] A. Rogalski, Infrared detectors, 2nd Edition, CRC Press, Boca Raton, FL, 2011.

[42] P. Capper, J. Garland (Eds.), Mercury Cadmium Telluride. Growth, Properties and Applications, John Wiley & Sons, Chichester, U.K., 2011.

[43] M. Vallone, M. Goano, F. Bertazzi, G. Ghione, R. Wollrab, J. Ziegler, Modeling photocurrent spectra of single-color and dual-band HgCdTe photodetectors: Is 3D simulation unavoidable?, J. Electron. Mater. 43 (8) (2014) 3070–3076. doi:10.1007/s11664-014-3252-9.

[44] N. K. Dhar, R. Dat, A. K. Sood, Advances in infrared detector array technology, in: S. L. Pyshkin, J. M. Ballato (Eds.), Optoelectronics. Advanced Materials and Devices, InTechOpen, Rijeka, Croatia, 2013, Ch. 7, pp. 149–190. doi:10.5772/51665.

- simulation of HgCdTe infrared detectors with realistic alloy composition profiles essential for their optimization
- realistic full-wave electromagnetic with compositionally-graded layers is difficult with commercial simulators
- we give practical hints for discretizing the grading into sublayers
- we test several different discretizations
- we assess when the grading may be neglected

Declarations of interest: none